

# Shallow Rupture of the 2011 Tarlay Earthquake ( $M_w$ 6.8), Eastern Myanmar

by Yu Wang,\* Yu-Nung Nina Lin, Mark Simons, and Soe Thura Tun

**Abstract** We use L-band Advanced Land Observation Satellite PALSAR data to infer the distribution of subsurface fault slip during the Tarlay earthquake ( $M_w$  6.8) in eastern Myanmar. We find the total length of surface rupture is approximately 30 km, with nearly 2 m maximum surface offset along the westernmost section of the Nam Ma fault (the Tarlay segment). Finite-fault inversions constrained by Interferometric Synthetic Aperture Radar (InSAR) and pixel-tracking data suggest that fault slip is concentrated within the upper 10 km of the crust. Maximum slip exceeds 4 m at a depth between 3 and 5 km. Comparison between field measurements and near-fault deformation obtained from the InSAR range-offset result suggests about 10%–80% of displacement occurred within a 1 km wide zone off the main surface fault trace. This off-fault deformation may explain the shallow slip deficit that we observed during this earthquake. We estimate a recurrence interval for Tarlay-like events to be 1600–6500 yrs at this section of the Nam Ma fault. A detailed paleoseismological study is essential to clarify the slip behavior and the earthquake recurrence interval of the Nam Ma fault.

## Introduction

Although major tectonic faults in the Indochinese peninsula have been mapped (e.g., [Le Dain \*et al.\*, 1984](#); [Lacassin \*et al.\*, 1998](#)), we have little understanding of their rupture characteristics, including their average rupture recurrence intervals, the depth of the seismogenic zone, and the spatial and temporal variation in seismic and aseismic slip behavior. Several  $M \sim 7$  earthquakes occurred in the central part of Indochina during the late twentieth century (e.g., the  $M_w$  7.0 Lancang–Gengma earthquakes in 1988 and the  $M_w$  6.8 Myanmar–China earthquake in 1995), but the distribution of fault slip in these events was not well constrained by data. Thus, the 24 March 2011  $M_w$  6.8 Tarlay earthquake (also known as the Mong Hpayak earthquake) provides a unique opportunity to infer faulting behavior in the Golden Triangle area between Myanmar and Laos.

The Tarlay earthquake occurred at the westernmost section of the Nam Ma fault (Fig. 1), with a coseismic surface rupture extending more than 17 km along the previously mapped Nam Ma fault trace ([Tun \*et al.\*, 2014](#)). Associated surface rupture was partially mapped in the field by the Myanmar Earthquake Committee about two weeks after the main-shock. However, because of limited road access in the field and diffuse surface deformation in several regions, the extent of fault offset was only measured at limited locations. Thus,

satellite-based Interferometric Synthetic Aperture Radar (InSAR) imagery provides key observations revealing the pattern of coseismic ground deformation and surface displacements across the ruptured section of the Nam Ma fault. We exploit the InSAR data to constrain a finite-fault source model, which in turn helps further our understanding of faulting behavior in the Golden Triangle region.

We use both InSAR and pixel-tracking techniques to estimate different components of ground deformations associated with the Tarlay earthquake. We compare these ground deformations with the fault offset measurements from a post-earthquake survey. We then invert for the distribution of fault slip on a model of the Nam Ma fault plane and use this model to explore the behavior of shallow fault slip during the Tarlay earthquake. We conclude by estimating possible earthquake recurrence scenarios of the Nam Ma fault system, assuming the earthquake represents the characteristic event along the Nam Ma fault.

## The Nam Ma Fault and the 2011 Tarlay Earthquake

The Nam Ma fault forms part of a major left-lateral fault system in the northern Sunda block between Myanmar and Laos (Fig. 1). Although its fault trace lies in the Golden Triangle area where field investigation has been nearly impossible due to logistical concerns, this 215 km long structure has been mapped from the interpretation of satellite imagery and the 90 m Shuttle Radar Topography Mission (SRTM) digital

\*Now at Earth Observatory of Singapore, Nanyang Technological University, Singapore 639798, Republic of Singapore.

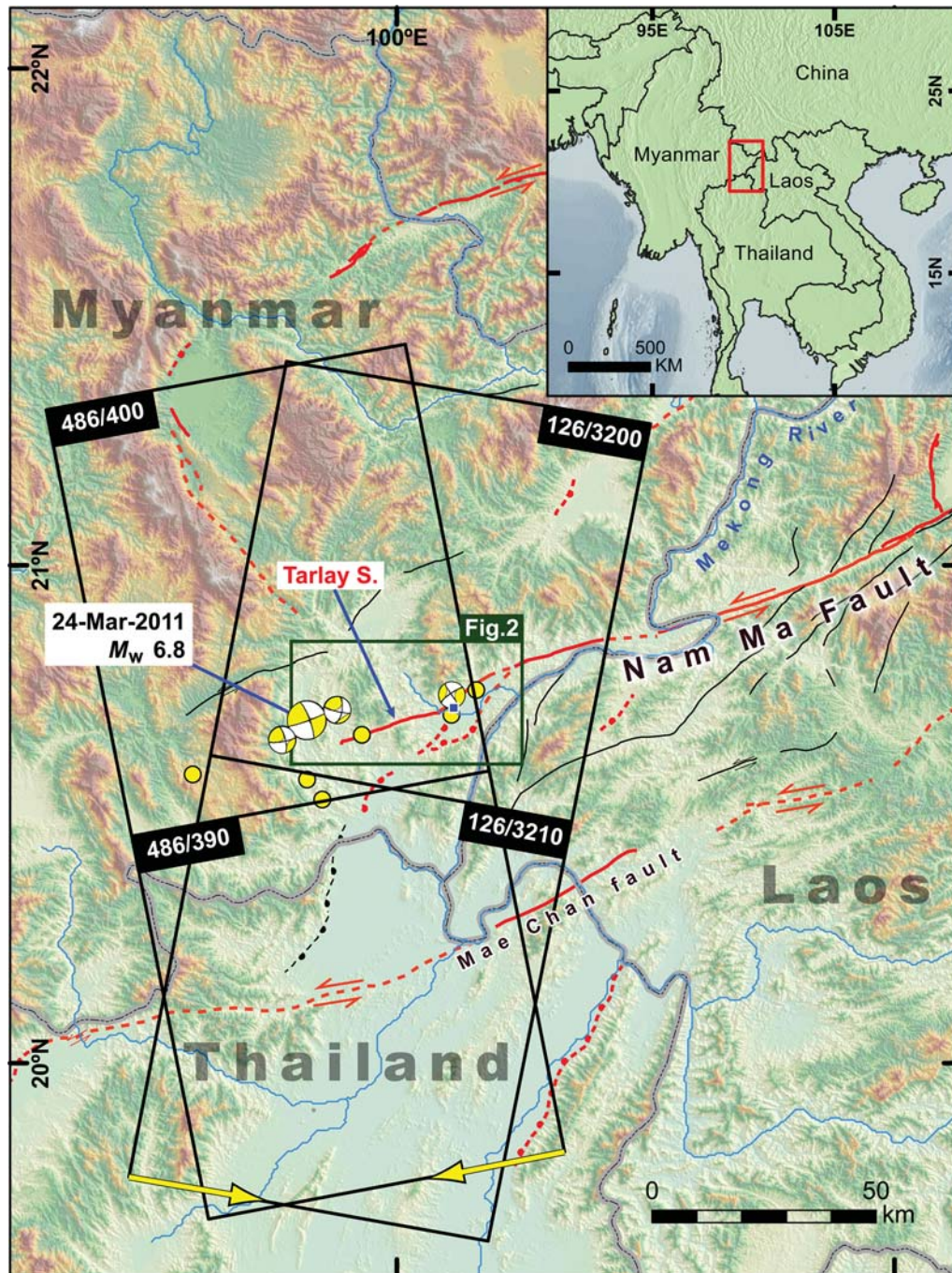


**Figure 1.** The 24 March 2011 Tarlay earthquake ( $M_w$  6.8) occurred along the western edge of the Nam Ma fault system, located near the Myanmar–Laos border. Centroid moment tensor solutions are for the mainshock and major aftershocks. Other aftershocks of smaller magnitudes are indicated by yellow circles. The black boxes outline the footprint of the Advanced Land Observation Satellite (ALOS) L-band Synthetic Aperture Radar data used in this study, with the line-of-sight (LOS) vectors in yellow arrows. The red lines are the active (solid) and suspect active (dashed) strike-slip faults mapped from the 90 m Shuttle Radar Topography Mission (SRTM) shaded relief imagery with assistance from published geological maps (e.g., [Bender and Bannert, 1983](#)). The black lines are the bedrock faults that do not show associated active geomorphic features from the digital elevation model. The small blue rectangle at the center of this map shows the location of Tarlay township, which is the major city along the western Nam Ma fault. Country borders are shown in gray lines.

elevation model (DEM) (e.g., [Lacassin et al., 1998](#)). In the central portion of the Nam Ma fault, the Mekong River forms a hairpin loop where the river flows across the fault trace (Fig. 1) ([Lacassin et al., 1998](#)). This geomorphic feature suggests the

Nam Ma fault was once a right-lateral fault before slip reversal of the Red River fault and was subsequently reactivated as a left-lateral fault with an estimated average slip rate of 0.6–2.4 mm/yr ([Lacassin et al., 1998](#)).



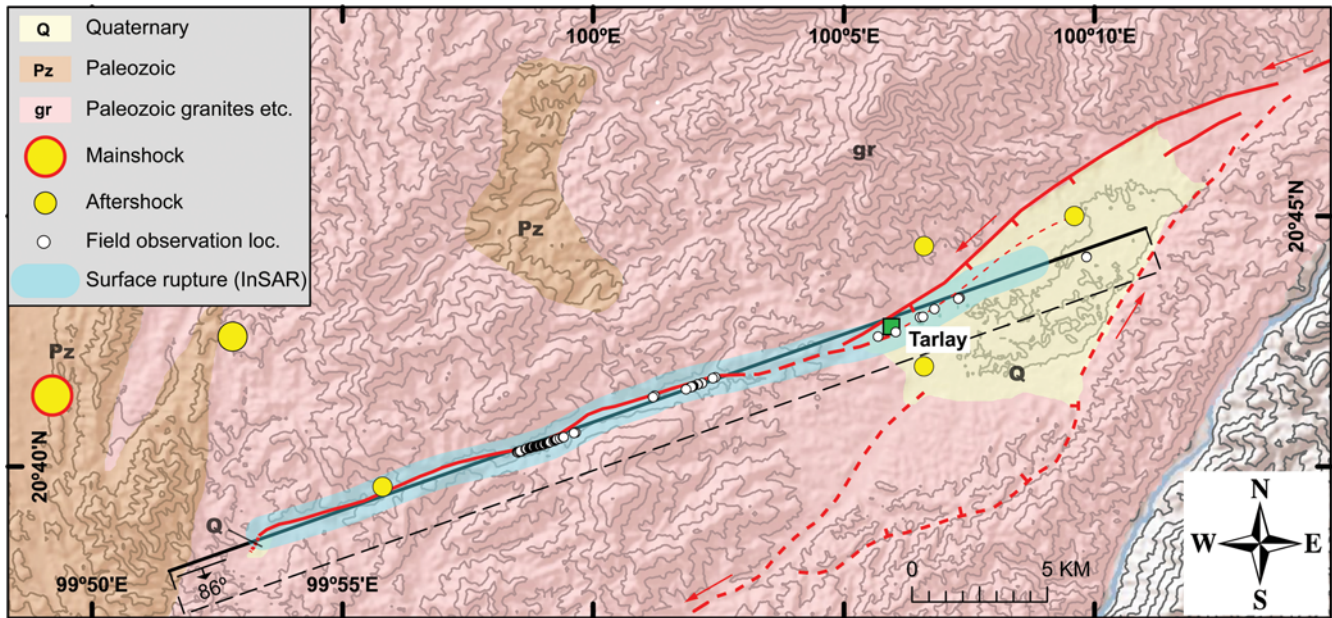


**Figure 2.** Detailed mapping of the Tarlay segment at the westernmost section of the Nam Ma fault, based on the 90 m SRTM and 15 m Landsat imagery. Most of the fault trace transects through the granitic formation (gr), with its western termination close to the Paleozoic sedimentary rocks (Pz; Bender and Bannert, 1983). The white dots are the locations of surface rupture that Myanmar geologists found in the field (Tun *et al.*, 2014). In general, the surface rupture locations match the fault trace that we mapped from remote sensing datasets. The black rectangle indicates the southward-dipping fault plane that we used in the dislocation model. Its surface trace is referenced to the field investigation results and our mappings.

Along the western end of the Nam Ma fault in remote eastern Myanmar, the fault trace exhibits classical horsetail geometry, suggesting that this fault system transitions from a single fault zone to a diffuse zone with several subparallel fault segments. The Tarlay segment is one of these fault segments at the western end of the Nam Ma fault. This segment runs N70°E east of the Tarlay Township, transecting the hilly area west of the Mekong River (Figs. 1 and 2). To the west, our interpretation from the 90 m SRTM DEM suggests the Tarlay segment terminates at a small tectonic basin within the mountains (marked by Q in Fig. 2). To the east, a triangle-shaped transtensional basin appears in which the trace of the Tarlay segment propagates straightly into the basin (Fig. 2). Active tectonic features gradually disappear along the Tarlay segment within this transtensional basin, whereas a series of triangular facets and offset alluvial fans reappear along the main Nam Ma fault trace that bounds the northern margin of the basin. These observations imply the presence of a left stepover between the Tarlay segment and the main trace of the Nam Ma fault, where transfer of slip northward creates a releasing bend along the northern part of the basin.

The inferred epicenter of the 24 March 2011 Tarlay earthquake ( $M_w$  6.8) from the National Earthquake Information Center (NEIC) catalog falls very close to the western end of the Tarlay segment (Fig. 1). Most fault-plane solutions suggest this earthquake occurred on a nearly vertical fault with purely left-lateral slip (see Data and Resources). These solutions match our general concept of the slip sense and orientation of the Nam Ma fault. Epicenters of aftershocks

from the NEIC catalog from March to April 2011 also encircle the Tarlay segment (Fig. 1). Postearthquake field investigation revealed coseismic left-lateral offsets in the central part of the segment. In the transtensional basin at the eastern end, the rupture pattern becomes more complicated, suggesting near-surface distributed deformation (Tun *et al.*, 2014). We use Advanced Land Observation Satellite (ALOS) PALSAR L-band satellite imagery to derive a more complete view of surface rupture and to estimate the distribution of fault slip at depth.

### InSAR Data

From 2007 to 2011, the Japanese ALOS PALSAR L-band sensor acquired radar imagery permitting measurement of coseismic ground deformation in regions where dense vegetation usually causes decorrelation in shorter wavelength InSAR imagery (e.g., C-band and X-band). For the Tarlay earthquake, ALOS acquired pre- and postearthquake Synthetic Aperture Radar (SAR) images along ascending track 126 and descending track 486 that cover the westernmost section of the Nam Ma fault (Fig. 1, Tarlay segment). The pre- and post-earthquake data are about two months apart (Table 1). This relatively small interval of time helps to minimize the effects of temporal decorrelation.

We use the repeat orbit interferometry processing package ROI\_PAC (Rosen *et al.*, 2004). Both ascending and descending images suffer from decorrelation near the trace of the Nam Ma fault; nevertheless, they still show clear ground

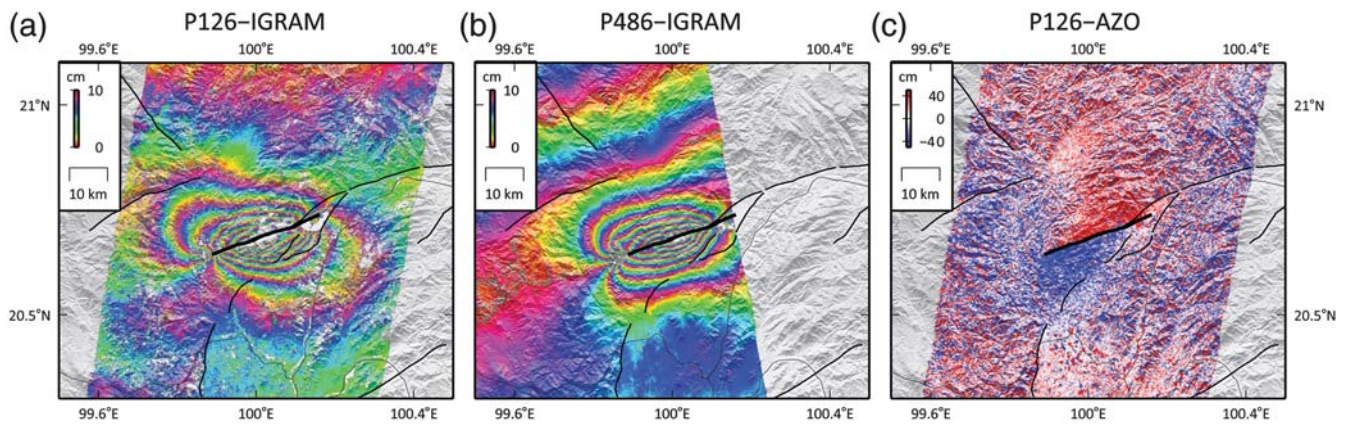


**Figure 3.** (a, b) ALOS L-band Interferometric Synthetic Aperture Radar (InSAR) and (c) pixel-tracking analysis results. The offset map of P126-AZO shows the ground deformations along the azimuth direction (AZO), whereas the other two InSAR results are the deformation along their LOS directions (Fig. 1). The bold black line shows the trace of the Tarlay segment mapped from SRTM and Landsat imagery. The other thin black lines are the regional faults that did not rupture during this earthquake.

deformation around the Tarlay segment (Fig. 3a,b). Both interferograms show simple concentric fringes around the fault without any complicated bifurcations. The pattern suggests a relatively simple geometry for faulting at the surface. The termination pattern around the western and eastern end of the fault looks somewhat different. To the west, fringes merge into the tip of the fault trace, implying that the fault earthquake rupture extends to the western end of the Tarlay segment, about 9 km west of the westernmost field surveyed point (Figs. 2 and 3a,b). To the east, fringes bend into the fault trace at an angle, suggesting that coseismic slip gradually decreases toward the eastern fault termination. A large area of decorrelation in the descending track coincides with the location of the transtensional basin. We believe this area of decorrelation suggests a plausible distributed deformation zone or that strong secondary ground deformation (e.g., liquefaction and slope failure along the riverbank) took place inside the basin (Fig. 3a).

We also applied the pixel-tracking analysis on the SAR amplitude data for descending track 126 to further constrain near-field deformation and to provide an additional component of deformation. The pixel-tracking technique produces deformation images with a higher level of noise, and therefore multilooking (spatial averaging) is usually necessary to improve the signal-to-noise ratio. We caution that some deformation features, in particular the sharp discontinuity across the fault trace, may be lost during this process.

Figure 3c shows the component along the azimuth direction (AZO) of the pixel-offset estimates. Although data from pixel tracking are noisier than InSAR in which fringes are visible, they allow deformation estimates in the near field where the interferograms completely decorrelate. From the western to the central part of the segment, the near-field data show a sharp deformation pattern across the fault. To the east, the boundary between opposite-moving displacements neither follows our pre-mapped Tarlay segment (Fig. 3c) nor matches the field observation result. This mismatch again suggests either secondary ground deformation effects (e.g., liquefaction) took place inside the basin or the fault slip during the earthquake did not form a localized rupture trace near the surface. We also note that we did not find any evidence of surface rupture along the northern boundary of this transtensional basin, suggesting that surface rupture did not extend beyond the Tarlay segment.

We carried out the same pixel-tracking analysis on scenes from ascending track 486. Because its line-of-sight (LOS) direction is almost parallel to the direction of the surface rupture, and given that this event is almost purely strike slip, the signal in the azimuth direction is small compared with the noise level. Therefore, we do not include this set of AZO observations in our model, but instead use the range offset (RAO) result for validation. RAOs and interferometric measurements measure the same LOS component of the deformation field, so the information they provide is redundant

Table 1  
Advanced Land Observation Satellite PALSAR Data Used in This Study

	Path	Frame	Pre-Earthquake Date (yyyy/mm/dd)	Scene ID	Postearthquake Date (yyyy/mm/dd)	Scene ID
Ascending track	486	390	2011/02/16	ALPSRP269800390	2011/04/03	ALPSRP276510390
	486	400	2011/02/16	ALPSRP269800400	2011/04/03	ALPSRP276510400
Descending track	126	3200	2011/02/14	ALPSRP269433200	2011/04/01	ALPSRP276143200
	126	3210	2011/02/14	ALPSRP269433210	2011/04/01	ALPSRP276143210



(Figs. 3b and 4). However, RAOs are less influenced by decorrelation, can sometimes better resolve displacements near the fault, and do not need to be phase unwrapped. Using these data, we estimate near-fault deformation within a  $\pm 500$  m window across the fault (Fig. 4). We compare these near-fault observations with both the predictions of shallow fault slip in our inferred model and the fault offset data from the field survey.

### The Slip Distribution of Tarlay Earthquake

Using both the ascending and descending InSAR data, plus the AZO observations from the descending track, we estimate the distribution of subsurface fault slip on the Tarlay segment. To improve model efficiency, we adopt a spatially variable data resampling/averaging approach based on the estimation of the inherent data resolution for a given source model (Lohman and Simons, 2005). This approach reduces the total number of data points to  $< 1000$ , while preserving the essential information contained in the original data (Fig. 5).

Our fault model has a general strike of  $N70^\circ E$ , similar to the strike of the observed surface rupture and the premapped Tarlay segment from SRTM data (Fig. 2). Because no well-located aftershock data are available in this area, we adopt the dip angle of  $86^\circ$  southeast (SE) from the Global Centroid Moment Tensor solution, which agrees with the field observation of the southern side of the Tarlay segment as the down-thrown side (Tun *et al.*, 2014). We discretized the fault plane into  $1 \text{ km} \times 0.6 \text{ km}$  rectangles from the surface to 12 km depth. We use elastic Green's functions based on a homogeneous elastic half-space model with a Poisson's ratio of 0.25.

We regularize the solution using a Laplacian damping term and further control the solutions by minimizing total potency of the inferred model. The degree of smoothing and potency constraint is chosen through an L-curve (Fig. 6). We computed an ensemble of models with different combinations of regularization weighting parameters ( $\lambda_1$  for smoothing and  $\lambda_2$  for potency constraint) and plot the values of reduced chi-square ( $\chi_{re}^2$ ) as a function of  $\lambda_1$  and  $\lambda_2$ . We use two criteria to choose our best model: (1) the intersection between the knees of the  $\chi_{re}^2$  plane along the  $\lambda_1$  and the  $\lambda_2$  directions and (2) the proximity of reduced  $\chi^2$  to unity, in which model errors equal to observation errors. We also tested the necessity of the total potency constraint and found that if we remove that constraint, slip tapers toward the lower left corner of the fault plane (Fig. 6e). If we allow the fault to extend deeper, this tapering pattern goes all the way down to whatever is the maximum depth of the given fault model. This tapering pattern is thus the result of overfitting long-wavelength noise in our dataset, and therefore we consider the slip potency constraint as a necessary regularization term to minimize this artifact.

Our selected model (Fig. 6b) fits the data well in general, although some systematic pattern appears in the residuals (Fig. 5). We then carried out a grid search to obtain the opti-

mized dip angle to figure out whether the systematic pattern results from this specific issue. However, the improvement of goodness of fit is marginal between our current dip angle ( $86^\circ$  SE) and the best solution ( $87^\circ$  SE), with only 0.2% decrease in the root mean square residual. The systematic pattern does not vanish in all 21 planar fault models that we tested (from  $80^\circ$  SE to  $90^\circ$  at  $0.5^\circ$  increment). It hence is likely that the fault plane is curved instead of purely planar or that some secondary fault in the flower structure of the Tarlay segment has been active during this event, although there is no sign on the surface of such a structure.

Our preferred coseismic model (Fig. 7) is almost purely left lateral with a minimal dip-slip component. This result matches field observations, in which most surface ruptures also appear to be purely left lateral (Tun *et al.*, 2014). The inferred slip occurs within the upper 10 km of the crust, in which the major slip patch concentrates between depths of 2.5 and 6 km, with a maximum slip of nearly 4.5 m at the central part of this depth range. The region of high slip is centered close to the western part of the fault plane, with its slip decreasing faster to the west than to the east.

Toward the eastern and western end of the rupture, our preferred model shows different slip behavior near the termination of the fault. To the east, the slip patch extends smoothly upward, forming a narrower and shallower rupture patch beneath the basin, and gradually diminishes at shallow depths ( $< 3$  km in depth). In contrast, at the western end of the fault, the depth distribution of fault slip retains a similar width toward its western termination. The model also suggests that fault slip decreases rapidly at the western end of the Tarlay segment, from 3 m to  $< 1$  m beneath the western termination of the premapped surface fault trace (Fig. 7).

Both our preferred model and the measurement from RAO data suggest the rupture broke the surface along the entire Tarlay segment. The amount of slip near the surface is small compared with the maximum fault slip at 2.5–6 km in depth. Thus, our model suggests a significant reduction in slip within the topmost 2 km of crust, in which coseismic slip decreases from 4 m at 3 km deep to about 1 m near the surface (Fig. 7).

Near the central part of the fault, offsets measured in the field and the modeled shallow slip are roughly consistent with each other. Further east, the agreement between the shallow slip and the field measurements is not as close (Fig. 7b). This section is also where pixel offset data are too noisy for us to obtain measurable near-fault deformation. The modeled shallow slip shows larger amplitude of surface slip than measured in the field. We attribute this difference to the finite size of our topmost fault patches and mapping of any diffuse deformation (off-fault deformation) onto the single fault plane.

Using the reference value of the shear modulus of the Earth's crust (30–33 GPa), we infer a geodetic moment on the order of  $1.6 \times 10^{19} - 1.8 \times 10^{19}$  N·m, corresponding to  $M_w$  6.8, in agreement with the NEIC moment magnitude estimated from the global seismic network. Effects of

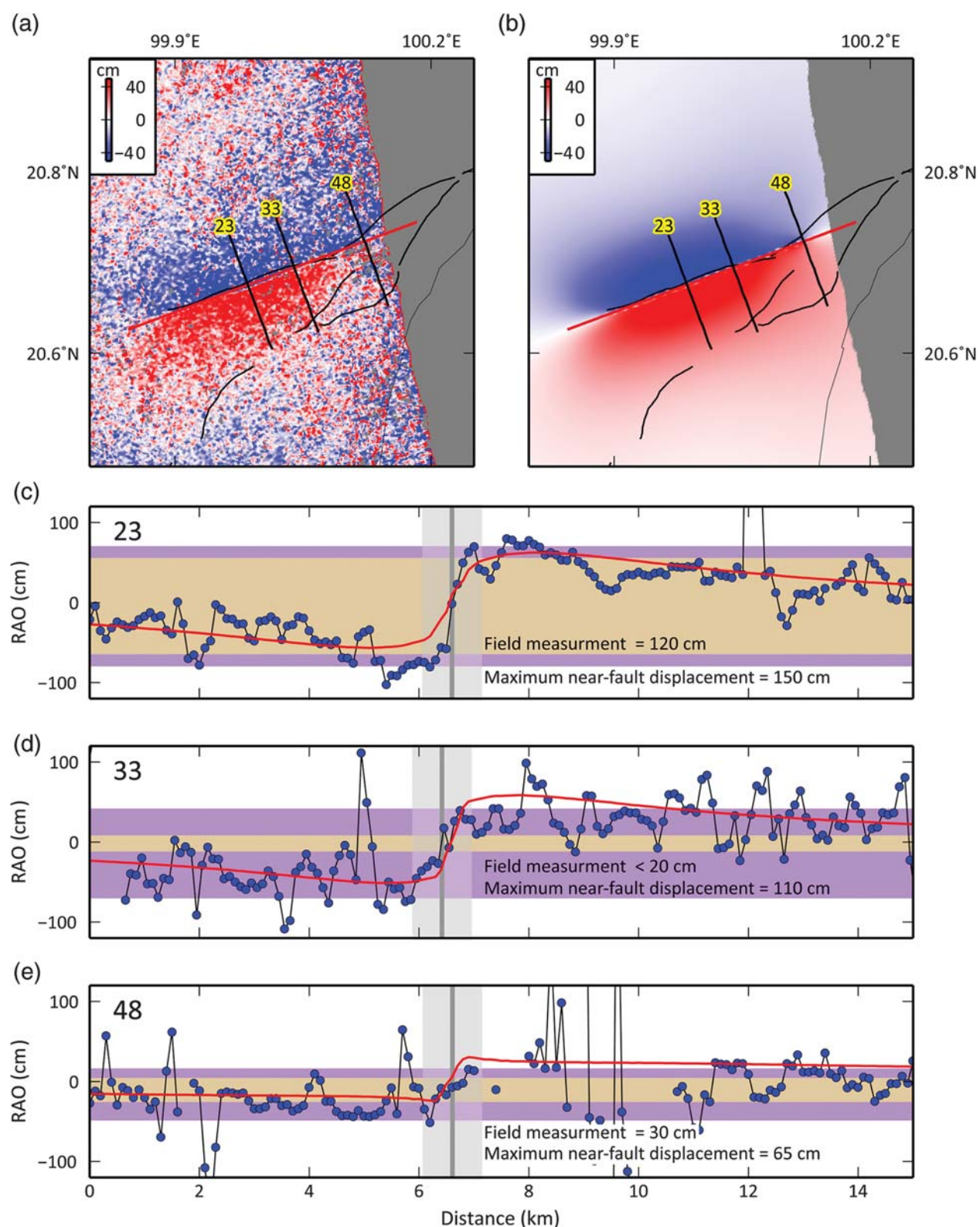


**Figure 4.** (a) The range offset (RAO) for descending track 486 and (b) the prediction from our preferred finite-fault model. The RAO data have been processed with multilooking (spatial averaging) to improve the signal-to-noise ratio. The resolution for both the RAO data and the modeled results is 90 m. The deformation component of the RAO data is almost parallel to the strike of the fault, so here the RAO results are directly compared with the field measurements. (c) Ground deformation along profile 23 (blue dots) and the modeled deformation (red line). The width of the brown area indicates the amount of offset during field measurements at the same location, whereas the width of the purple region indicates the maximum near-fault displacement reading from the RAO data. (d) Ground deformation along profile 33, showing a more distributed deformation across the fault. (e) Ground deformation along profile 48.

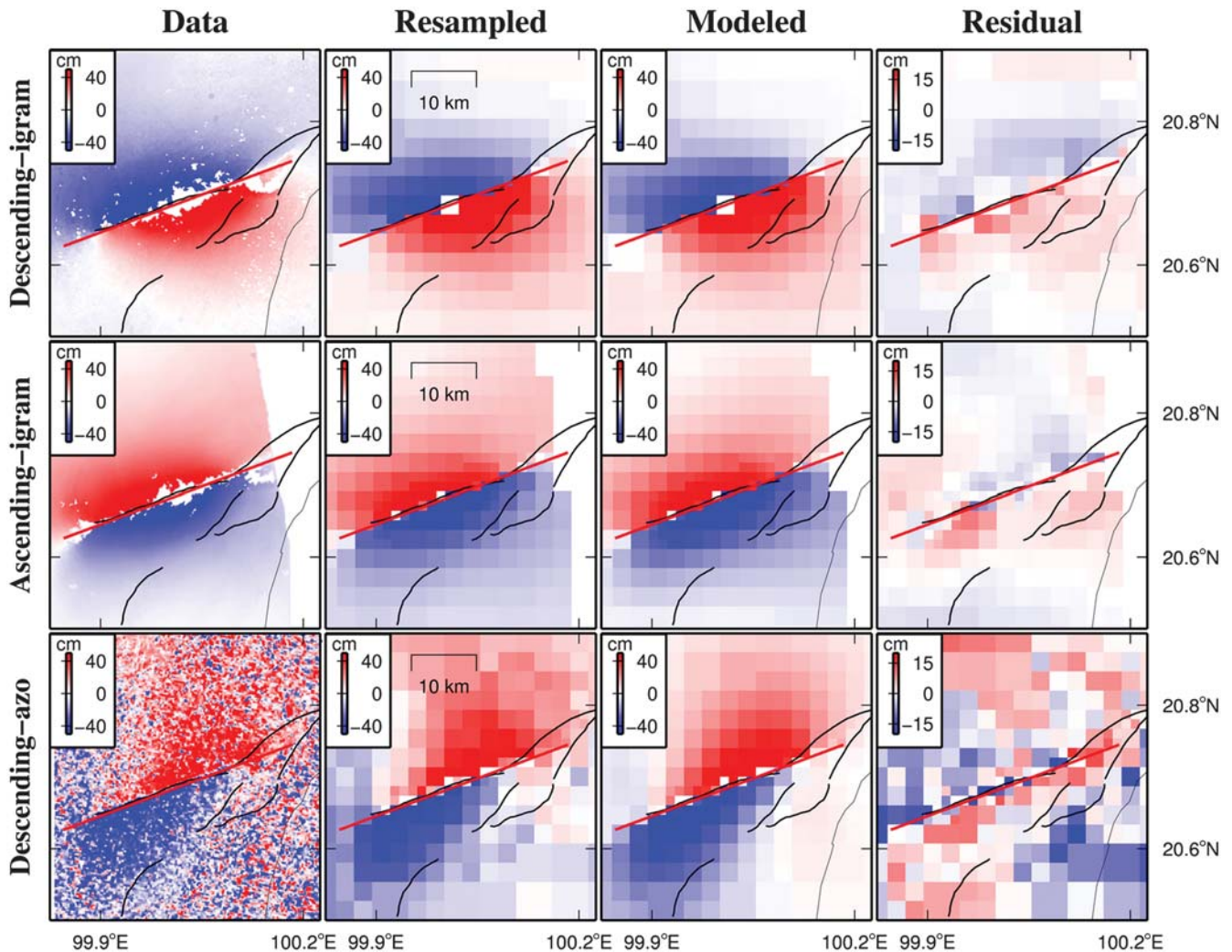


**Figure 5.** We resample all three ground deformation fields before inverting for the fault-slip distribution. Generally, the modeled deformation fields match the InSAR and pixel-tracking data with a single planar fault. The residuals show some systematic pattern, which does not vanish even with the optimized dip angle ( $87^\circ$  SE). This pattern suggests that the fault plane may be curved rather than purely planar or that some secondary structure in the flower structure of the Tarlay segment has been active during the earthquake, although there is no sign of such a structure on the surface.

postseismic deformation may be included in our model, but we expect the influence to be small due to the short time interval ( $< 10$  days) between the earthquake and the post-earthquake SAR images.

## Discussion

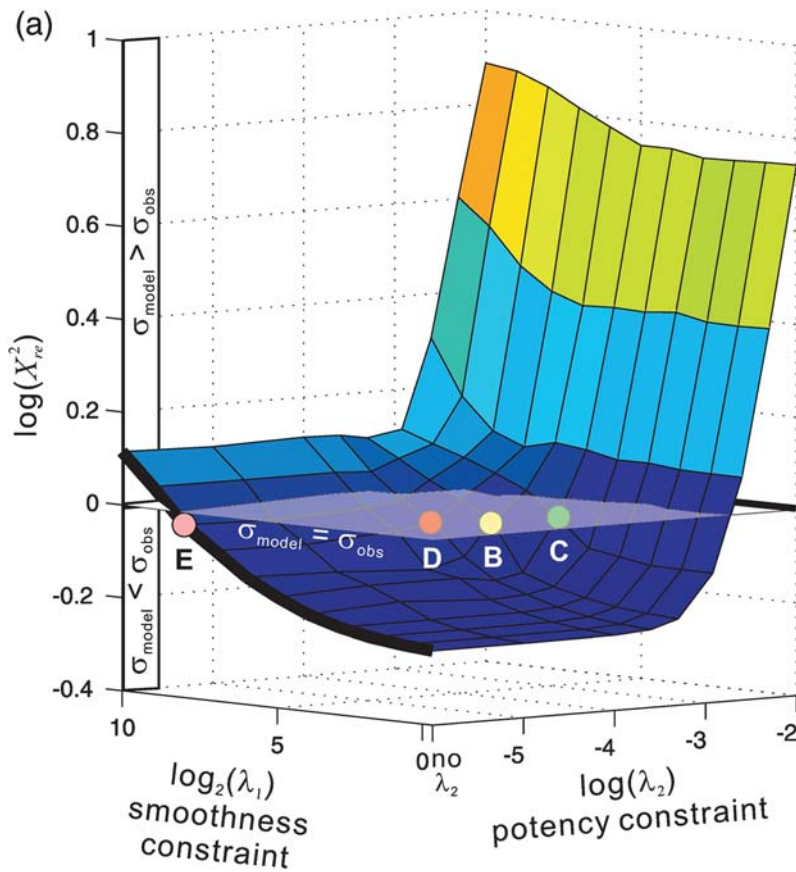
### Characteristics of the Surface Rupture

Pixel-tracking and InSAR observations indicate the entire length of the Tarlay segment ruptured during the March 2011 earthquake, as also hypothesized from field investigations (Tun *et al.*, 2014). Both slip on the uppermost row of slip patches in our preferred model and the near-fault deformation measured from RAOs suggest a broad bell-shaped pattern of surface rupture with a peak value of 1.5–2 m (Fig. 7). We find that near-fault deformation does not always

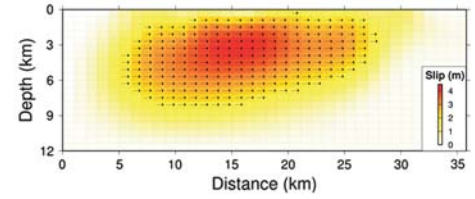
occur within a narrow zone of the surface rupture (Fig. 4). In some places, there is a clear sigmoidal pattern as one traverses the fault, the width of which varies along strike. We select three profiles to compare on-fault and off-fault deformation. We assume that field measurements represent actual on-fault displacement and the pixel offsets capture the total near-fault deformation.

Profile 23 demonstrates an end member in which most of the deformation concentrates along the fault surface rupture (Fig. 4c). The sharp sigmoidal pattern over a short distance in the profile suggests that most of the ground deformation occurred on the fault. Nevertheless, we still find about 10–30 cm more displacement from the pixel offsets than from the field measurements, suggesting a plausible 10%–20% of deformation occurred over distances of  $\sim 800$  m across the rupture. Because this 10–30 cm difference is very close to the measurement precision of the pixel-tracking analysis, the real

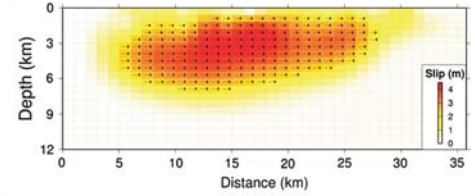




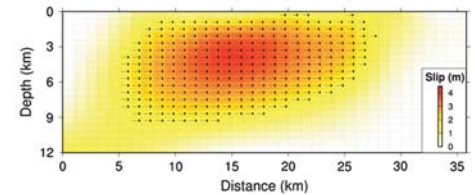
(b) Best model



(c) Rougher model



(d) Smoother model



(e) No potency constraint

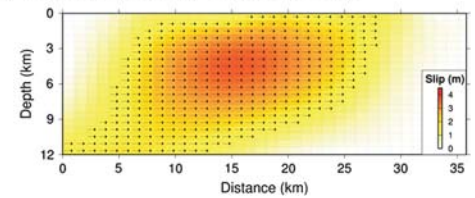


**Figure 6.** (a) The reduced chi-square ( $\chi^2_{re}$ ) plot as a function of the regularization weighting parameters ( $\lambda_1$ , model smoothness constraint;  $\lambda_2$ , for total potency constraint). (b–e) Different realizations of models. The best model is chosen based on the L-curve knees and on the proximity of  $\chi^2_{re}$  values to unity.

off-fault deformation could be even less. In fact, the field survey found a narrow rupture zone only along this section (Tun *et al.*, 2014).

Toward the east, profile 33 shows a different type of deformation near the main fault trace (Fig. 4d). This profile reveals a more gentle sigmoidal deformation pattern compared with profile 23, but the overall near-fault deformation remains large (approximately 1.1 m). Such a gentle deformation curve suggests that either rupture failed to reach the surface or that slip is distributed over a wide damage zone composed of multiple small fault planes. Field observations indicate a series of aligned en echelon cracks on the ground along this section of the fault, suggesting that deformation on the main fault trace is no more than 10–20 cm near the surface (Tun *et al.*, 2014). Field investigation also found several plausible fissures within a range of several hundreds of meters away from the fault near this profile. The lateral extensions of these plausible fissures were difficult to trace. Based on these geologic observations, we argue distributed slip can explain the gentle deformation pattern. However, it is difficult to tell whether these deformations mainly occurred along

different secondary faults in the damage zone or formed as dragging and warping in the country rocks around the main fault.

Further east, profile 48 is located within the transtensional basin (Fig. 4e). This profile again shows a gentle sigmoidal deformation pattern across the fault similar to profile 33. Field observations report offset rice paddy-field boundaries within the disrupted fields, where the maximum offset is 20–30 cm, compared with 40–65 cm of near-fault deformation. Thus, we suggest that tectonic deformation off the main fault along profile 48 is up to 30 cm within the 1 km zone across the fault, accounting for ~50% of the total displacement.

Field measurements within the basin area are consistently lower than near-fault deformation from the pixel-tracking result (Fig. 7b), indicating possibly extensive off-fault deformation in the basin. Off-fault deformation may be attributed to the lower brittle strength of the saturated fluvial sediments that fill the basin. By comparison, off-fault deformation is less significant near the central part of the fault in general, where the fault trace transects a granitic



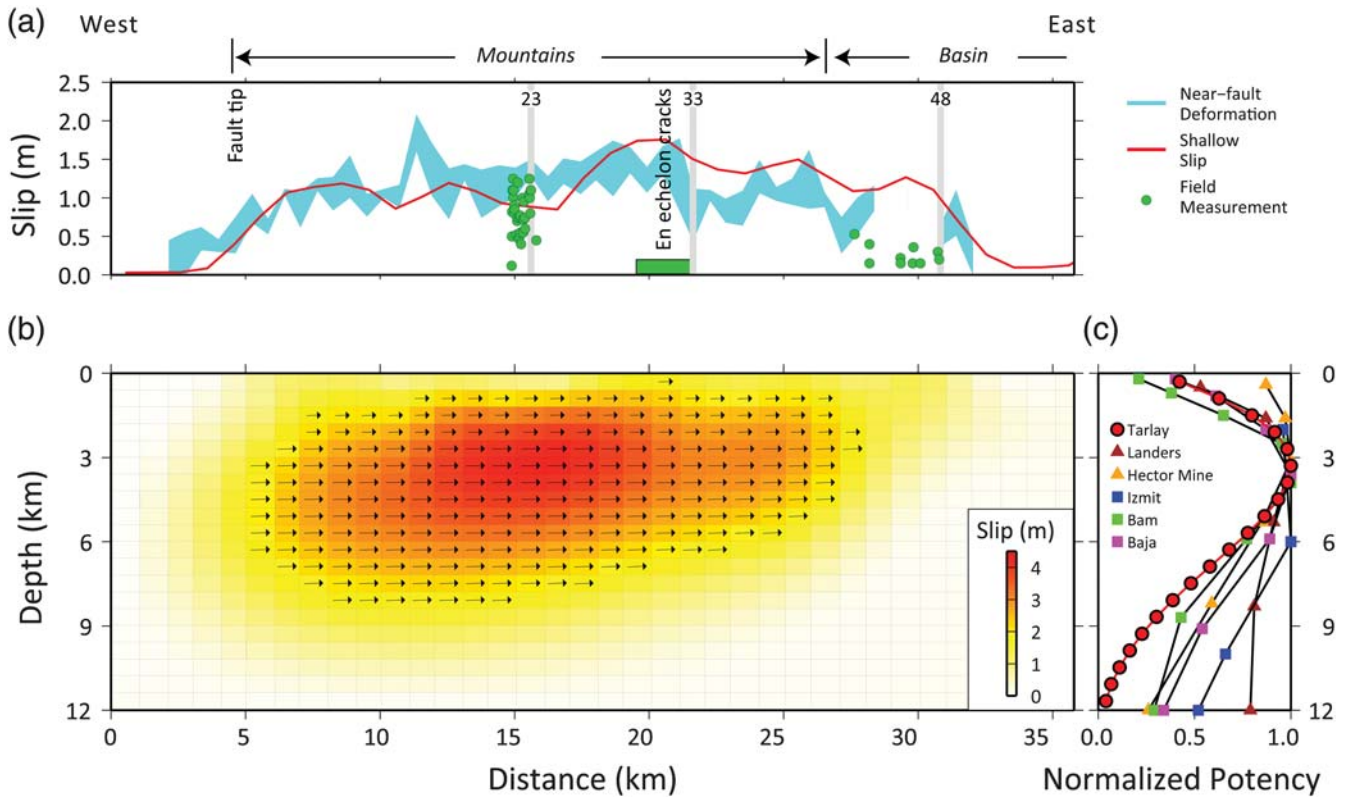


**Figure 7.** (a) Comparison between field measurements (green dots), the upper 600 m fault slip (red line), and the near-fault deformation measured from the AZO pixel-tracking analysis (Fig. 4, cyan) along the Tarlay segment. This figure shows a generally good match between the model result, the near-fault displacement, and the field investigation result at the central part of the fault. To the east in the basin area, both the field measurements and the near-fault displacement are systematically smaller than the modeled shallow slip. (b) The distribution of fault slip along the Tarlay segment. The maximum fault slip in our model is slightly larger than 4 m at 2.5–5 km depth. Most of the slip occurred at depths shallower than 10 km. (c) The comparison of the normalized slip potency from our preferred model (red dots) and other earthquake events (from Kaneko and Fialko, 2011). Slip potency of the Tarlay earthquake shows a depth-dependence profile very similar to the Landers earthquake and the Baja earthquake: all three events reach their maximum slip potency at about 3 km at depth, and their potency gradients at shallow depth are also identical.

batolith with only a thin alluvial layer mantled on top. This difference suggests that lithology, or the condition of the country rocks, may be a key factor controlling the fraction of off-fault deformation during an earthquake.

#### Shallow Slip Deficit

The apparent deficit of shallow slip in our preferred slip model is similar to that seen in many other magnitude  $\sim 7$  strike-slip fault events (e.g., Simons *et al.*, 2002; Fialko *et al.*, 2005, 2010; Sudhaus and Jónsson, 2011). Figure 7c illustrates the comparison of normalized slip potency as a function of depth between the Tarlay event and other studied earthquakes (e.g., Simons *et al.*, 2002; Fialko *et al.*, 2005; Kaneko and Fialko, 2011). We find the shallow slip deficit of the Tarlay earthquake resembles that of the 1992 Landers earthquake and the 2010 Baja earthquake. Among these three events, the shallow slip deficit is up to 50%–60%, and the potency gradients in the top 2–3 km layer are identical.

Although the cause of such shallow slip deficit has not been conclusively identified, simulations reveal several

possible sources for this phenomenon. Kaneko and Fialko (2011) suggest part of this deficit results from inelastic deformation near the Earth's surface, especially when the country rock's cohesion is low. Such inelastic slip can further enhance the inference of a slip deficit when we try to fit the inelastic ground deformation via the purely elastic model (e.g., Simons *et al.*, 2002; Barbot *et al.*, 2008; Kaneko and Fialko, 2011).

In the case of the Tarlay earthquake, we see plausible off-fault sympathetic deformation ranging from 10% to 80% of the total near-fault deformation at different locations (Fig. 4c–e). It seems reasonable to attribute the cause of the shallow slip deficit to inelastic off-fault deformations along the fault. However, although we are seeing a large degree of variation in the deformation off the main fault, we do not find an obvious relationship with the inferred shallow slip deficit at any given location. This discordance may result from (1) errors both in the observations and in the models, (2) the variation in off-fault deformations being only superficial, or (3) off-fault deformation and the shallow slip deficit achieving the balance only in the context of multiple earthquake

cycles rather than a single event. Despite this ambiguity, we emphasize the importance of recognizing along-strike variations of both aforementioned behaviors and the comparison with geological observations, which in turn may allow us to unravel the enigma of shallow slip deficit in the future.

#### Inferred Recurrence Interval on the Tarlay Segment

The difference between the maximum fault slip at depth and the maximum fault offset on the surface makes a significant difference when we estimate the average recurrence interval of earthquake from the coseismic fault offset data. If the fault slip during the Tarlay earthquake represents the characteristic slip pattern of the Tarlay segment, we can roughly estimate its recurrence interval by dividing its maximum fault slip with its average long-term slip rate. Lacassin *et al.* (1998) suggested the slip rate of the Nam Ma fault is 0.6–2.4 mm/yr, based on the channel offset of the Mekong River and the regional tectonic history. Therefore, if the 4 m fault slip at depth represents the characteristic slip on the Tarlay segment, the average recurrence interval of a Tarlay-earthquake-like event is about 1600–6500 yrs along this segment. Such frequency is three times lower than the estimation from the maximum surface offset (1.25 m), in which the interval decreases to the 600–2300 yr range (Tun *et al.*, 2014). The large variation in these first-order estimates of recurrence interval emphasizes the need for paleoseismological studies. As many strike-slip faults produce sequential and clustered events within a short period of time (e.g., North Anatolian fault, Stein *et al.*, 1997; Sagaing fault, Yeats *et al.*, 1997), we cannot at present conclusively estimate seismic hazard along the Nam Ma fault.

#### Conclusions

We have successfully conducted the InSAR and pixel-tracking analyses from ALOS PALSAR L-band dataset. The deformation pattern suggests a simple linear fault plane, with the eastern end submerged into the transtensional basin. Our slip inversion model suggests the entire 30 km long Tarlay segment ruptured during the 2011 earthquake. The rupture has a narrow and concentrated region of slip in the shallow part of the crust (< 10 km), with the peak slip at 2.5–6 km. Fault slip in the topmost 600 m layer reveals a broad bell-shape slip pattern and generally agrees with field observations and near-fault deformation measured from the pixel-tracking data.

By comparing the field survey result and the near-fault deformation, we find 10%–80% of the ground deformation occurred outside the main surface rupture. Such off-fault deformation is likely to be inelastic and may be the cause of shallow slip deficit that we observed in our slip model.

Given the average slip rate of 0.6–2.4 mm/yr on Nam Ma fault, we estimate the recurrence interval at the Tarlay segment to be 1600–6500 yrs. This estimate is three times greater than the estimate from the maximum surface offset. A detailed paleoseismological study of the Nam Ma fault is

essential to clarify the regional seismic-hazard potential in the golden triangle area.

#### Data and Resources

Epicepters of the mainshock and aftershocks were collected from the U.S. Geological Survey (USGS)/National Earthquake Information Center Preliminary Determination of Epicepters catalog (last accessed December 2011). The centroid moment tensor (CMT) solution of the mainshock was obtained from the USGS significant earthquake archive (<http://earthquake.usgs.gov/earthquakes/eqinthenews/2011/usc0002aes/#scitech>; last accessed March 2012). Global CMT solutions of aftershocks were collected from the Global CMT project database ([www.globalcmt.org/CMTsearch.html](http://www.globalcmt.org/CMTsearch.html); last accessed December 2011). Advanced Land Observation Satellite data are copyrighted by the Japanese Aerospace Exploration Agency and Ministry of Economy, Trade, and Industry (METI) and are provided through the U.S. Government Research Consortium Data Pool at the Alaska Satellite Facility.

#### Acknowledgments

We have benefited greatly from discussions with Kerry Sieh and Paul Tapponnier. The comments from Roland Bürgmann and an anonymous reviewer greatly helped us to improve the quality of the manuscript. This research is supported by the National Aeronautics and Space Administration, Grant Number NNX12AO30G, and by the Earth Observatory of Singapore (EOS). This is EOS Contribution Number 48, Caltech Tectonics Observatory Contribution Number 219, and Caltech Seismological Laboratory Contribution Number 10091.

#### References

- Barbot, S., Y. Fialko, and D. Sandwell (2008). Effect of a compliant fault zone on the inferred earthquake slip distribution, *J. Geophys. Res.* **113**, no. B06404, doi: [10.1029/2007JB005256](https://doi.org/10.1029/2007JB005256).
- Bender, F. K., and D. N. Bannert (1983). *Geology of Burma*, Gebrüder Borntraeger Verlagsbuchhandlung, Science Publishers, Berlin, Germany.
- Fialko, Y., A. Gonzalez, J. J. Gonzalez-Garcia, S. Barbot, S. Leprince, D. T. Sandwell, and D. C. Agnew (2010). Static rupture model of the 2010  $M$  7.2 El Mayor-Cucapah earthquake from ALOS, ENVISAT, SPOT and GPS data, *Eos Trans. AGU* **91**, T53B–2125.
- Fialko, Y., D. Sandwell, M. Simons, and P. Rosen (2005). Three-dimensional deformation caused by the Bam, Iran, earthquake and the origin of shallow slip deficit, *Nature* **435**, 295–299.
- Kaneko, Y., and Y. Fialko (2011). Shallow slip deficit due to large strike-slip earthquakes in dynamic rupture simulations with elasto-plastic off-fault response, *Geophys. J. Int.* **186**, 1389–1403.
- Lacassin, R., A. Replumaz, and P. H. Leloup (1998). Hairpin river loops and slip-sense inversion on southeast Asian strike-slip faults, *Geology* **26**, 703–706.
- Le Dain, A. Y., P. Tapponnier, and P. Molnar (1984). Active faulting and tectonics of Burma and surrounding regions, *J. Geophys. Res.* **89**, 453–472.
- Lohman, R. B., and M. Simons (2005). Some thoughts on the use of InSAR data to constrain models of surface deformation: Noise structure and data downsampling, *Geochem. Geophys. Geosyst.* **6**, Q01007, doi: [10.1029/2004GC000841](https://doi.org/10.1029/2004GC000841).
- Rosen, P. A., S. Hensley, G. Peltzer, and M. Simons (2004). Updated repeat orbit interferometry package released, *Eos Trans. AGU* **85**, 47.
- Simons, M., Y. Fialko, and L. Rivera (2002). Coseismic deformation from the 1999  $M_w$  7.1 Hector Mine, California, earthquake as inferred from InSAR and GPS observations, *Bull. Seismol. Soc. Am.* **92**, 1390–1402.



- Stein, R. S., A. A. Barka, and J. H. Dieterich (1997). Progressive failure on the North Anatolian fault since 1939 by earthquake stress triggering, *Geophys. J. Int.* **128**, 594–604.
- Sudhaus, H., and S. Jónsson (2011). Source model for the 1997 Zirkuh earthquake ( $M_w = 7.2$ ) in Iran derived from JERS and ERS InSAR observations, *Geophys. J. Int.* **185**, 676–692, doi: [10.1111/j.1365-246X.2011.04973.x](https://doi.org/10.1111/j.1365-246X.2011.04973.x).
- Tun, S. T., Y. Wang, S. N. Khaing, M. Thant, N. Htay, Y. M. M. Htwe, T. Myint, and K. Sieh (2014). Surface ruptures of the  $M_w$  6.8 March 2011 Tarlay earthquake, eastern Myanmar, *Bull. Seismol. Soc. Am.* **104**, doi: [10.1785/0120130321](https://doi.org/10.1785/0120130321)
- Yeats, R. S., K. E. Sieh, and C. R. Allen (1997). *The Geology of Earthquakes*, Oxford University Press, New York.

Division of Geological and Planetary Sciences  
California Institute of Technology  
1200 E. California Boulevard  
Pasadena, California 91125  
wangyu79@gps.caltech.edu  
(Y.W., Y.-N.N.L.)

Seismological Laboratory  
Division of Geological and Planetary Sciences  
California Institute of Technology  
1200 E. California Boulevard  
Pasadena, California 91125  
(M.S.)

Myanmar Earthquake Committee  
Myanmar Engineering Society  
MES Building  
Hlaing Universities' Campus  
Hlaing Township  
Yangon 11052, Myanmar  
(S.T.T.)

Manuscript received 27 December 2012;  
Published Online 14 October 2014